Ultra-Low-Profile Continuous Transverse Stub Array for SatCom Applications

Michele del Mastro, Adham Mahmoud, Thomas Potelon, Ronan Sauleau, Gilles Quagliaro, Anthony Grbic, Mauro Ettorre

This article has been accepted for publication in a future issue of this journal, but has not been fully edited. Content may change prior to final publication. Citation information: DOI 10.1109/TAP.2022.3142369, IEEE Transactions on Antennas and Propagation

Ultra-Low-Profile Continuous Transverse Stub Array for SatCom Applications

Michele Del Mastro, Adham Mahmoud, Thomas Potelon, Ronan Sauleau, *Fellow, IEEE*, Gilles Quagliaro, Anthony Grbic, *Fellow, IEEE*, Mauro Ettorre, *Senior Member, IEEE*

***Abstract*—Modern K/Ka-band satellite communications have become increasingly demanding in recent years with regard to the performance of the terminal antenna used in the link. These terminals should be high-gain and broadband, as well as guarantee polarization diversity over a large field-of-view. A low-profile is also highly desired to integrate the antenna system into a variety of moving platforms such as aircraft and trains. An ultra-low-profile continuous transverse stub array is proposed here to tackle these challenges. The antenna array is realized in printed circuit board technology by adopting a contactless transition between the stacked-up layers without resorting to blind or buried vias. The proposed antenna is wideband (impedance matched within the band 19-31 GHz, i.e., $\sim 50\%$) and provides multi-beam radiation for polar angles as far as $\pm 22.5^\circ$. The peak value of the gain is 19.7 dBi and the maximum radiation efficiency equals 50%. Furthermore, the antenna array is combined with a dual-band polarization converter. The latter provides orthogonal circular polarization in two non-adjacent bands. The overall antenna system performs right- and left-hand circular polarization within the SatCom down- and up-links in the K/Ka-band, respectively. For each polarization, the axial ratio is below 3 dB over 9.47% and 4.42% fractional bandwidths, respectively.**

***Index Terms*—Ultra-low-profile, SOTM, wideband, dual-circular polarization, PCB technology, dual-band polarizer, periodic structures, metasurface, LP-to-CP conversion, SatCom.**

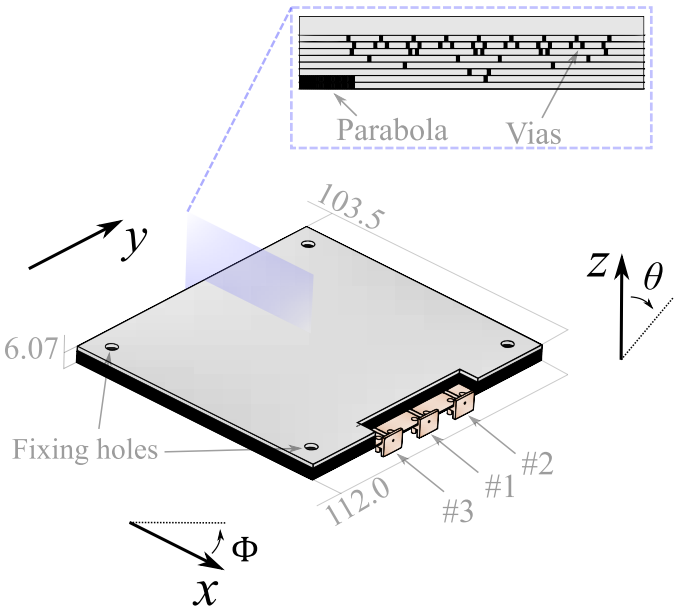

Fig. 1: Perspective view of the antenna architecture with the stack-up shown. Dimensions are given in millimeters.

I. Introduction

THE ever-increasing demand for high data-rate wireless networks has prompted the development of advanced satellite communication (SatCom) technologies. Future generations of SatCom systems will employ satellites orbiting in low Earth orbits. By deploying them in constellations, a permanent and global coverage of the Earth's surface can be provided. As a consequence, ground antennas must track the operating satellite while flying at high angular velocities [1], [2].

For high-throughput satellite systems, modern SatCom terminal antennas are also required to operate over large bandwidths. A large range of SatCom links for civilian applications is currently allocated at K- and Ka-bands [3]. More precisely, the 17.3-21.2 GHz band is associated with the down-link frequency channel, whereas the 27.5-31 GHz band is reserved for the up-link. Usually used for civil applications, the sub-bands 19.2-21.2 GHz and 29-31 GHz will be here targeted as operative frequency ranges. In these two bands, circular polarization (CP) is a key asset to enhance link reliability and robustness for long-range signal transmissions. In addition, the antenna shall exhibit a low-profile to ease integration into moving platforms (e.g., trains, aircraft, etc.) in order to mitigate aerodynamic issues.

The continuous transverse stub (CTS) arrays stand out among existing solutions due to their broadband and wide-angle scanning performance [4]. When used in combination with a quasi-optical system [5], [6], they can provide electronically-controlled beam-steering in elevation and two-dimensional (2-D) scanning by means of an azimutal rotation of the antenna module. CTS arrays also exhibit a low-profile [7], [8]. However, this class of antennas suffers from being intrinsically linearly-polarized. Recent studies have overcome this limitation and proposed a solution achieving both circular [9]–[11] and dual-linear [12], [13] polarization by conceiving

Manuscript received XX/XX/2018; revised XX/XX/2018.

M. Del Mastro was with Univ. Rennes, CNRS, IETR (Institut d'Électronique et des Technologies du numéRique) - UMR 6164, 35000 Rennes, France. He is now with Anywaves, 31000 Toulouse, France (e-mail: michele.del.mastro@anywaves.eu).

A. Mahmoud, R. Sauleau, and M. Ettorre are with Univ. Rennes, CNRS, IETR (Institut d'Électronique et des Technologies du numéRique) - UMR 6164, 35000 Rennes, France (e-mail: michele.delmastro@univ-rennes1.fr).

T. Potelon is with Direction Générale de l'Armement, 35170 Bruz, France (e-mail: thomas.potelon@intradef.gouv.fr).

G. Quagliaro is with Thales SIX GTS France, 92230 Gennevilliers, France (e-mail: gilles.quagliaro@thalesgroup.com).

A. Grbic is with Radiation Laboratory, Department of Electrical Engineering and Computer Science, University of Michigan, Ann Arbor, MI 48109-2122 USA (e-mail: agrbic@umich.edu).

This article has been accepted for publication in a future issue of this journal, but has not been fully edited. Content may change prior to final publication. Citation information: DOI 10.1109/TAP.2022.3142369, IEEE Transactions on Antennas and Propagation

a multi-mode operation of the radiating slots with an *ad-hoc* engineered dispersion of the parallel plate corporate feed network. However, these antennas cannot radiate orthogonal CPs between receive (Rx) and transmit (Tx) SatCom channels. A simpler, as well as powerful, solution relies on combining a linearly-polarized CTS array with a dual-band polarizer [15]–[17] placed within the proximity of the antenna aperture.

This paper presents the design of an ultra-low-profile CTS array achieving a very broadband operation (about 50% fractional bandwidth) [14]. The antenna module is fully realized in printed circuit board (PCB) technology. As shown in Fig. 1, the antenna consists of 9 stacked dielectric substrates. A contact-less transition exploiting capacitive coupling is used to convey the electromagnetic energy from a PCB layer to another without resorting to buried or blind vias [18]. The resulting antenna profile is very thin (6.07 mm). The antenna also provide a moderate gain (the peak value is 19.7 dB) with a linearly-polarized radiation over the 19-31 GHz band. The scanning range of the antenna array has been designed to be $\pm 22.5^\circ$ in elevation by feeding the array with a quasi-optical system. Wider field-of-views can be easily achieved by further displacing the feeding horn along the focal plane of the quasi-optical system, or using other feeding mechanisms [19]. A prototype has been fabricated and tested at the Institute of Electronics and numeRical Technologies (IETR), Rennes, France. Afterwards, the antenna array was combined with the dual-band, orthogonally-polarized linear-to-circular polarization (LP-to-CP) converter presented in [17] to achieve orthogonal CPs in two non-adjacent bands. The overall antenna module radiates left-hand CP (LHCP) over the band 20.1-22 GHz, whereas right-hand CP (RHCP) radiation is provided within the band 28.8-30 GHz.

The paper is organized as follows. The design procedure and the antenna architecture are presented in section II. Section III describes the fabricated prototype and reports the experimental results of the self-standing antenna. The combine of module CTS array and dual-band polarizer [17] is detailed in section IV along with the measured results of the overall system. The conclusions are drawn up in section V.

II. Design Procedure and Antenna Performance

In this section, we introduce the design of the antenna array. Specifically, the electrical properties of the employed waveguide technology are first investigated in terms of dispersion and insertion losses (IL). Afterwards, the active reflection coefficient of these waveguides, arranged as open-ended radiating stubs in an infinitely-extended lattice, are studied. Finally, the overall antenna performance is characterized by means of full-wave simulations.

A. Substrate-integrated parallel-plate waveguide

A parallel-fed CTS array can be designed in PCB technology by replacing the continuous metallic walls of the open-ended parallel plate waveguides (PPW) with via fences. A three-dimensional (3-D) view of this type of PPW is illustrated in Fig. 2. The modes propagate in the positive z-axis direction. The structure resembles substrate integrated waveguide (SIW)

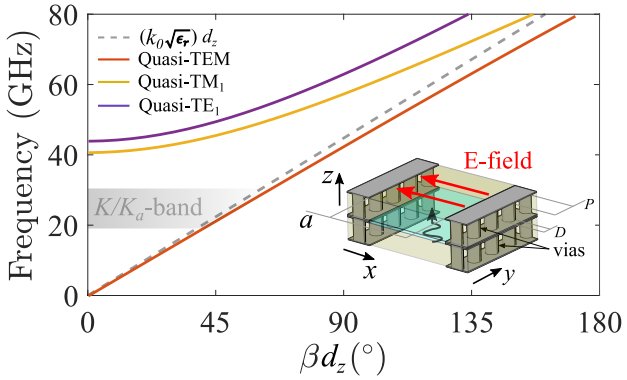

Fig. 2: Dispersion diagram of the SI-PPW. Geometrical parameters: $D = 0.3$ mm, $P = 0.6$ mm, $a = 2.13$ mm, $\epsilon_r = 2.2$, and $d_z = 1.1$ mm.

technology with a different propagation direction of modes, i.e., along the z-axis instead of the y-axis [see Fig. 2]. The SIW technology is well-established and exhaustively documented in the open literature [20]–[24]. As in standard SIW technology, the design of the periodicity P and diameter D of the vias is carried out to mitigate leakage. In the present case, full-wave simulations have been performed to achieve a good trade-off between feasibility and losses. Considering the Rogers RT/duroid 5880® ($\epsilon_r = 2.2$ and $\tan\delta = 0.0009$ @ 10 GHz) [25], the SI-PPW is designed having $D = 3$ mm and $P = 2D$. The laminated layers are glued together with the adhesive film Rogers® CuClad 6250 ($\epsilon_{r,glue} = 2.32$ and $\tan\delta_{glue} = 0.0013$ @ 10 GHz) whose pressed thickness is about 30 μm.

The dispersion diagram is plotted in Fig. 2. The geometrical parameters of the structure are listed in the caption of Fig. 2. As in standard PPWs, the SI-PPWs support a quasi transverse electromagnetic (TEM) mode. The dispersion curve of the quasi-TEM mode does not match exactly with the non-dispersive line, i.e., $k = k_0\sqrt{\epsilon_r}$ where k_0 is the free-space wavenumber. As a consequence, the mode propagating inside the SI-PPW is not a pure TEM wave, as the E-field lines are perturbed near the walls made of via fences. However, the structure exhibits mono-modal propagation in the band of interest [refer to the grey area in Fig. 2]. As shown in Fig. 2, the first transverse electric (TE_1) and magnetic (TM_1) modes are also supported but they are in cut-off within the band of interest.

Fig. 3(a) depicts the cross-sectional view of the SI-PPW and the simulated ILs are reported in Fig. 3(b). As shown in Fig. 3(b), the ILs are of three kinds: ohmic, dielectric, and those due to leakage. The ohmic losses originate from the copper (thickness 0.035 mm and conductivity $\sigma = 5.8\times10^7$ S/m) used for the metallic parts of the antenna. There is also field leakage due to the bonding layer, placed between two consecutive substrates [refer to the light-blue color in Fig. 3(a)], and to the space between vias. The leakages are reduced by tuning the copper plates, placed in a mushroom-like configuration on the top of each via [see Fig. 3(a)]. The most critical ILs are given by leakages. Moreover, the dielectric ILs are more critical than the ohmic ones. In general, the total ILs range from 0.028 to 0.063 dB in the frequency range 19-31 GHz.

This article has been accepted for publication in a future issue of this journal, but has not been fully edited. Content may change prior to final publication. Citation information: DOI 10.1109/TAP.2022.3142369, IEEE Transactions on Antennas and Propagation

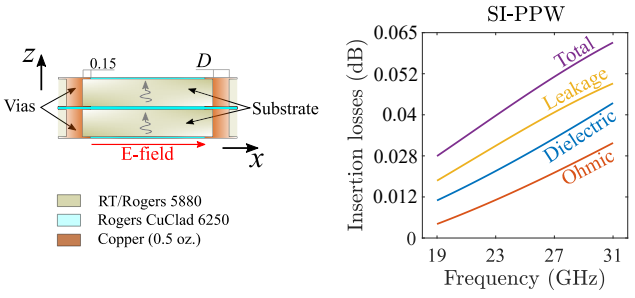

(a) Cross-section. (b) Insertion losses.

Fig. 3: (a) Cross-section of the SI-PPW in the xz-plane. (b) Simulated insertion losses for the SI-PPW. The vias diameter is $D = 3$ mm. All other dimensions are given in millimeters.

Note that the ILs increase with frequency as expected.

B. Radiating unit cell and corporate feed network

The design of the CTS array in PCB technology starts from defining its radiating unit cell. The simulation setup of the unit cell is shown in Fig. 4(a). An open-ended SI-PPW is fed from the bottom with a waveguide port [refer to Fig. 4(a)] and radiates into layered half free-space. The structure is arranged in a periodic environment defining long slots etched on a laminate substrate ($\epsilon_r = 2.2$ and thickness 0.508 mm). Geometrical details of the SI-PPW are reported in the caption of Fig. 4(a). The impedance matching is improved by placing a dielectric layer of thickness $l = 1.544$ mm on top of the aperture [28]. The cell is studied by means of full-wave simulations using CST Microwave Studio [26]. As shown in Fig. 4(a), periodic boundary conditions are enforced on the lateral faces of the array's radiating cell. A Floquet port is placed on the top of the radiating air box, whereas a waveguide port is located at the bottom-most face of the structure. The waveguide port is used to launch a TEM mode into the structure in such a way to radiate x-polarized E-fields. The simulated active reflection coefficient of the array's unit cell is plotted in Fig. 4(b) for different pointing angles θ_0 in the yz-plane (H-plane). The active reflection coefficient is lower than -15 dB, everywhere in the frequency band 19-31 GHz for broadside radiation. When scanning along with the H-plane, the impedance bandwidth remains roughly unvaried. The simulated results show that the reflection coefficient is below -13 dB across the band of interest for pointing angles as large as $\theta_0 = 30°$ along the H-plane. The simulations demonstrate the broadband capability of parallel-fed CTS arrays. Specifically, the achieved impedance bandwidth is larger than 48%.

The long radiating slots are parallel-fed by means of a corporate feed network (CFN) made of 1-to-2 way power dividers in SI-PPW technology. The design of the power dividers is realized using only two PCB layers for compactness and ease of fabrication. A drawing of the CFN is shown in Fig. 5 as it is seen in the cross-section along with the xz-plane. The antenna array consists of 8 radiating long slots parallel-fed by a CFN in SI-PPW technology. As it is depicted in Fig. 5, the CFN is designed using 7 substrates (S1 to S8) of

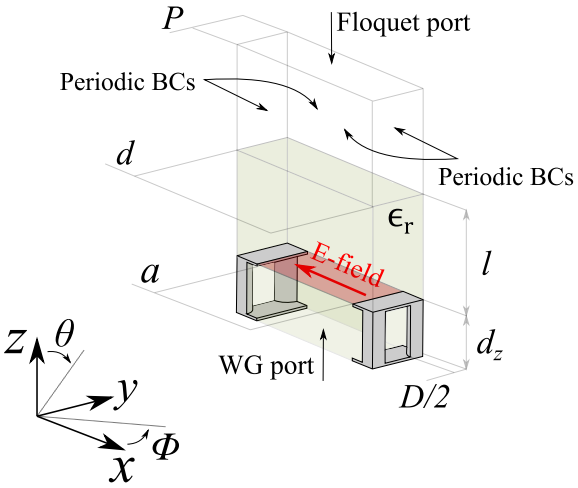

(a) Array's unit cell.

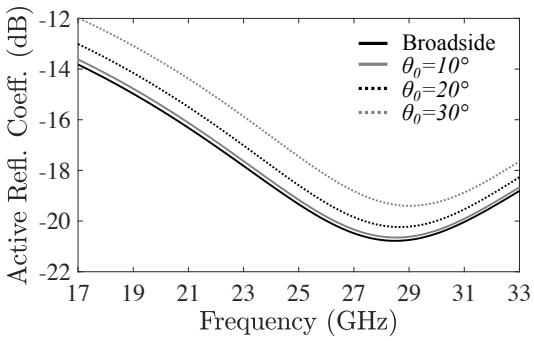

(b) Active reflection coefficient.

Fig. 4: (a) Simulation setup of the radiating cell of the CTS array in PCB technology. (b) Simulated active reflection coefficient of the array's unit cell. The results are shown for four beam directions along the yz-plane (H-plane). Geometrical parameters: $a = 2.13$ mm, $d = 2.73$ mm, $l = 1.544$ mm, $d_z = 0.508$ mm, $D = 0.3$ mm, $P = 0.6$ mm, and $\epsilon_r = 2.2$.

thickness 0.508 mm and one substrate S9 of thickness 1.544 mm employed as matching layer. The geometrical details of the structure along y-axis can be found in Fig. 4(a). Each power divider is realized with two substrates, connected to each other through coupling slots [see Fig. 5]. The geometrical details are reported in the caption of Fig. 5. The Poynting vector is also depicted across the structure to identify the electric paths traveled by the propagating waves. A quasi-optical system (pillbox coupler) is integrated into substrates S1 and S2 and realizes a continuous line source distributed along the y-axis. The parabola is designed using metallic vias of diameter 0.35 mm and periodicity 0.5 mm. The pillbox system is described in the section II-C. Since the structure is periodic by P [see Fig. 4(a)] along y-axis, full-wave simulations can be carried out for a single slice of the array. This setting allows to excite the structure with a waveguide port having uniform field distribution at the section AA' in Fig. 5.

The CFN was designed by means of an optimization procedure with the aim to minimize the reflection coefficient at section AA' [see Fig. 5]. By enforcing radiation boundary con-

This article has been accepted for publication in a future issue of this journal, but has not been fully edited. Content may change prior to final publication. Citation information: DOI 10.1109/TAP.2022.3142369, IEEE Transactions on Antennas and Propagation

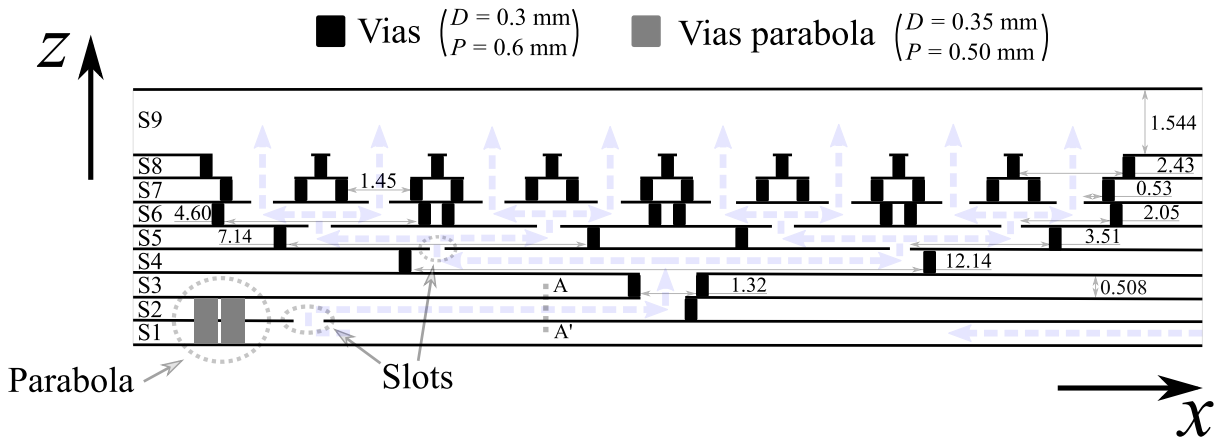

Fig. 5: Cross-sectional view (xz-plane) of the CFN in SI-PPW technology. The structure is periodic by P along y-axis [see Fig. 4(a)]. The blue arrows depict the Poynting's vector of the field propagating in the structure. Dimensions are in millimeters.

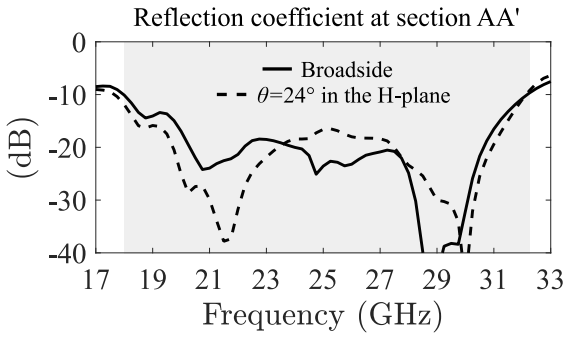

Fig. 6: Simulated reflection coefficient of the structure in Fig. 5. The results refer to section AA'.

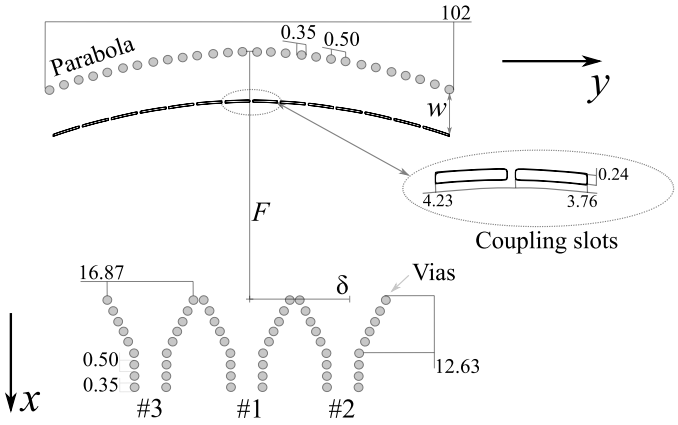

Fig. 7: Schematic of the quasi-optical system as seen from a top view. All the dimensions are given in millimeters.

ditions above the slots, the vias positions are swept along x-axis to achieve the desired matching. The reflection coefficient at section AA' is reported in Fig. 6. The -10 dB impedance matched band is extended from 18 to 32.2 GHz (about 62% of relative bandwidth). For broadside radiation, the reflection coefficient is below -20 dB almost everywhere in the band of interest, i.e., 19-31 GHz. In conclusion, the physical radiating aperture of the antenna array is about $8 \cdot 2.13$ mm $\times$ 102 mm $= 1738.08$ mm^2.

C. Pillbox beam-former in PCB technology

This section describes the quasi-optical system (pillbox coupler) employed to feed the CTS array. Fig. 7 illustrates the top view of the pillbox system. Two substrates, namely S1 and S2, are dedicated to its design [refer to Fig. 5]. As shown in Fig. 7, the parabola is realized with periodic vias (diameter 0.35 mm and period 0.50 mm) drilled through the substrates S1 and S2. The focal length of the parabola is $F = 60$ mm. Three input horns in SIW technology, located in the substrate S1, are used to illuminate the parabola. The horn displacement δ is linked to the scanning angle of the array θ_0 [6]. The corresponding scan angle for $\delta = 17.5$ mm is $\theta_0 = 22.5°$.

The horns in substrate S1 illuminate the parabolic reflector. The fields reflected by the parabola are coupled to substrate S2 through rectangular slots. The slots are etched into the metallic layers between substrates S1 and S2. They are placed at a distance $w = 3.4$ mm from the parabola [refer to Fig. 7]. Within substrate S2, the field has a planar wavefront and propagates along the x-axis.

The horns are linearly displaced along the focal length of the parabola. Their apertures are designed so to provide a -10 dB edge tapering of the field across the solid angle described by

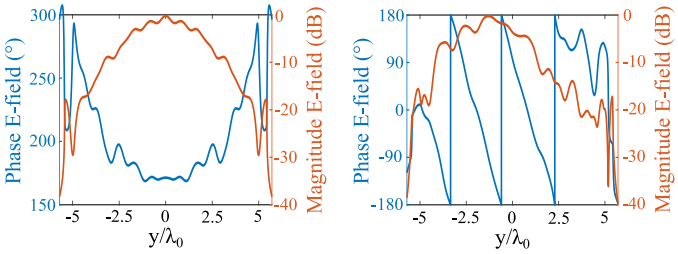

(a) Horn #1. (b) Horn #2.

Fig. 8: Simulated E-field in the substrates S2 as function of the the normalized position along y, when the parabola is illuminated by the horns (a) #1 and (b) #2. The radiating slots are centered at $y = 0$. λ_0 is the wavelength at 29 GHz.

This article has been accepted for publication in a future issue of this journal, but has not been fully edited. Content may change prior to final publication. Citation information: DOI 10.1109/TAP.2022.3142369, IEEE Transactions on Antennas and Propagation

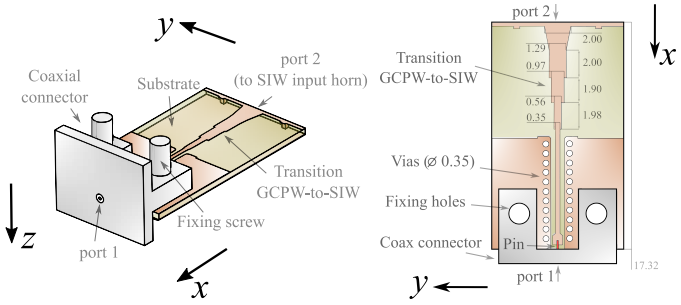

(a) Perspective view. (b) Top view.

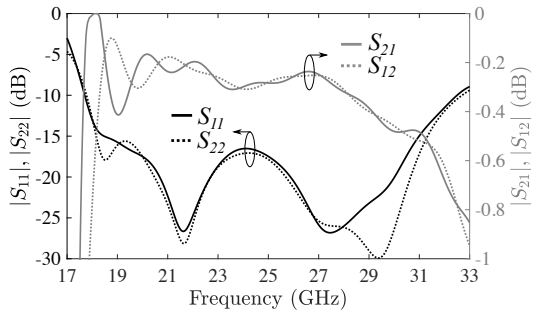

(c) S-parameters.

Fig. 9: Drawing of the coaxial-to-GCPW-to-SIW transition: (a) 3-D and (b) top view. (c) Simulated S-parameters. The orange color indicates copper, whereas the grey represents the connector's metal. The substrate is shown in green. All dimensions are given in millimeters.

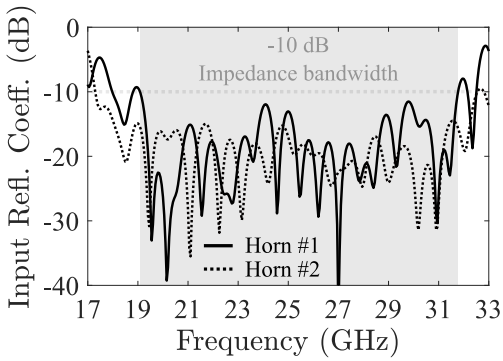

(a) Input reflection coefficient.

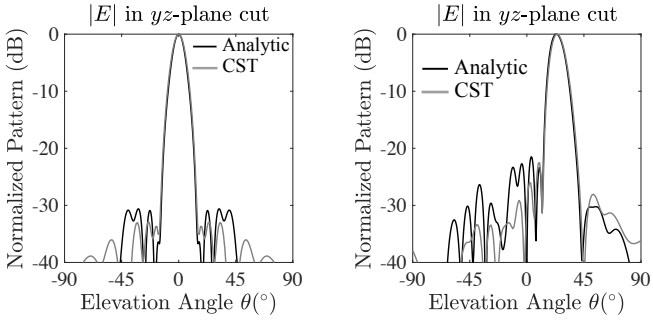

(b) Horn #1. (c) Horn #2.

Fig. 10: (a) Simulated input reflection coefficients. (b)-(c) Simulated radiation patterns at 25 GHz of the antenna for horn #1 and #2 excitations, respectively.

the reflector. The simulated results in Figs. 8(a) and (b) show the E-field distribution in the substrate S2 as a function of the normalized distance y/λ_0 (λ_0 is the free-space wavelength at 29 GHz) for horn #1 and #2 excitations, respectively. As shown in Fig. 8(a), the magnitude of the E-field is tapered at the edges of the parabola and the slots are illuminated by a field distribution having a flat phase response. This enables the array to radiate at bore-sight. On the contrary, the horn #2 provides a field distribution still having a tapered amplitude, but with a saw tooth-like phase behavior [see Fig. 8(b)]. The latter provides linear phasing of the long slots, thus enabling scanning along with the H-plane.

D. Coaxial-to-GCPW-to-SIW transition

The input section of the antenna consists of 50 Ω female coaxial connectors, namely Southwest 1092-01A-9 [42]. Three connectors are used to feed the horns in the focal plane of the pillbox system [see Fig. 1]. They are solder-less and mounted using fixing screws. For each connector, the pin has the standard diameter of 2.92 mm and is adjusted on a grounded co-planar waveguide (GCPW), thus creating an electric contact to feed the SIW horns via a GCPW-to-SIW transition. A perspective view of the antenna input section is shown in Fig. 9(a). The GCPW-to-SIW transition consists of a stepped impedance matching section in micro-strip technology. It was designed by means of a full-wave optimization in CTS Microwave Studio [26] to achieve a good impedance matching within the band of interest. The top view of the GCPW-to-SIW transition is depicted in Fig. 9(b). The pin is connected to a GCPW surrounded by vias to mitigate leakages. The stepped transition conveys the energy from the coaxial to the input horn in SIW technology. The simulated S-parameters of the transition are reported in Fig. 9(c). Both the reflection coefficients at port 1 and 2 are below -15 dB over the band 19-31 GHz. The ILs are lower than 0.5 dB in the same frequency band with an average value around 0.3 dB.

E. Performance of the antenna array

A 3-D view of the overall antenna architecture is depicted in Fig. 1. The antenna achieves multibeam radiation where each beam is associated with a coaxial connector. According to the selected connector, the antenna pointing directions (ϕ_0, θ_0) are $(90^\circ, 0^\circ)$ and $(90^\circ, \pm 22.5^\circ)$. Furthermore, the coaxial-to-GCPW-to-SIW transition is designed on the reverse side with respect to the main beam direction. This avoids pattern perturbations due to field leakage from the microstrip line in the GCPW-to-SIW transition.

The simulated input reflection coefficient of the antenna is plotted in Fig. 10(a) for horn #1 and #2. The simulations consider ohmic and dielectric losses, as well as the radiation leakage. A -10 dB impedance bandwidth is observed in the band 19-31.7 GHz (50%) for the excitation of horn #1. When the antenna is excited by horn #2, the impedance bandwidth is even larger. The in-focus position, in fact, gathers the largest amount of reflected power from the parabola.

This article has been accepted for publication in a future issue of this journal, but has not been fully edited. Content may change prior to final publication. Citation information: DOI 10.1109/TAP.2022.3142369, IEEE Transactions on Antennas and Propagation

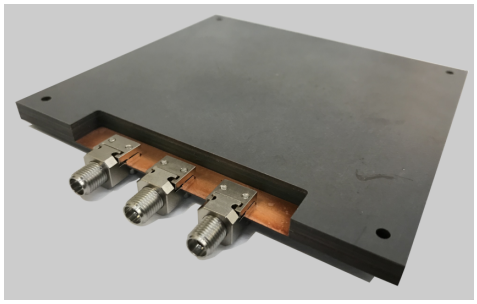

(a) Perspective view.

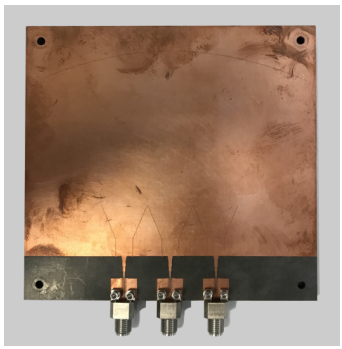

(b) Bottom view.

Fig. 11: Photographs of the fabricated prototype. (a) Perspective and (b) bottom side views.

The radiating performance can be predicted using the in-house tool reported in [9]. A finite-size array (comprising 170 array slices along y-axis) is considered. The calculated patterns are shown in Figs. 10(b) and (c) for excitations by horn #1 and #2 at 25 GHz, respectively. Excellent agreement is observed between the computed and simulated radiation patterns. Specifically, the side-lobe levels (SLL) are lower than -30 dB for broadside radiation and -22 dB when the antenna points at $\theta_0 = 22.5°$ in the H-plane.

III. Prototype and Experimental Results

The fabricated prototype is shown in Fig. 11. The vias are visible from the antenna bottom-side [see Fig. 11(b)] outlining the parabolic profile and the input SIW horns. The reflection coefficient of the antenna has been measured with a PNA network analyzer (Keysight N5227A). The measured results are shown in Fig. 12(a) under the excitation of horns #1, #2, and #3. The reflection coefficient is lower than -10 dB almost everywhere in the band of interest, i.e., 19-31 GHz, as expected from simulations.

The radiation patterns measured at 26 GHz in the H-plane are reported in Figs. 12(b) and (c). The measurements are in excellent agreement with full-wave simulations. In particular, the results in Fig. 12(b) refer to broadside radiation, whereas those in Figs. 12(c) to scanning. The SLLs are below -20 dB along the H-plane for broadside radiation [see Fig. 12(b)]. Also, the cross-polarized radiation is lower than -30 dB along with the same azimuth plane. Similarly, the radiation performance in scanning shows SLLs below -18 dB, as well as a cross-polarization level lower than -30 dB with respect to the peak value of the main beam [see Fig. 12(c)].

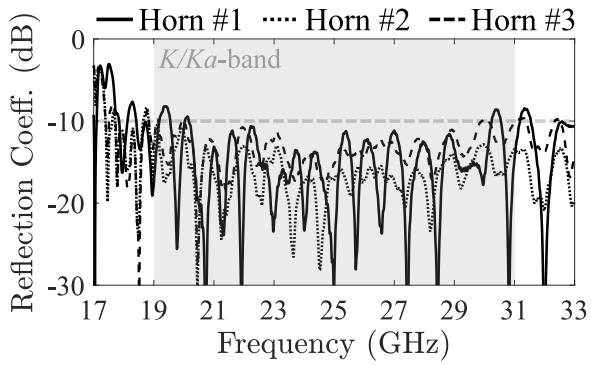

(a) Input reflection coefficient.

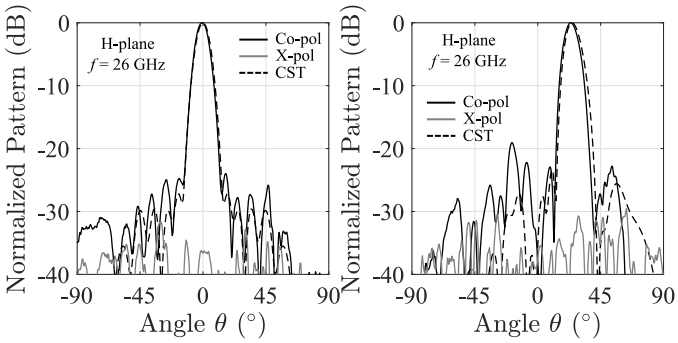

(b) Horn #1. (c) Horn #2.

Fig. 12: (a) Measured reflection coefficients. (b)-(c) Measured normalized patterns along the H-plane at 26 GHz.

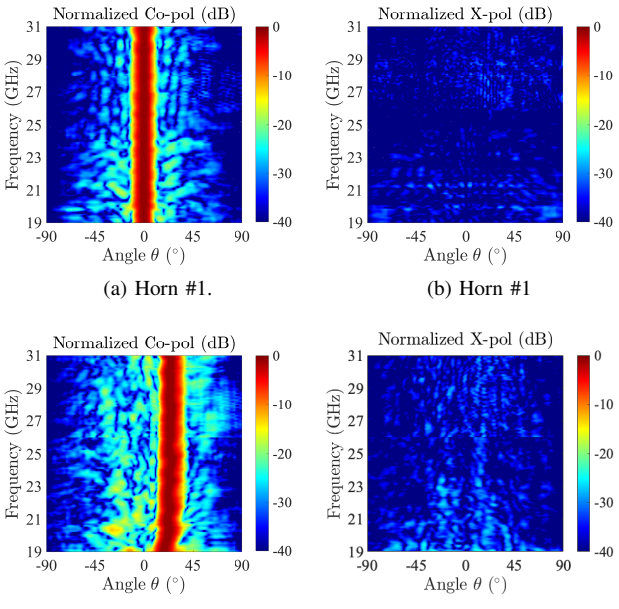

(a) Horn #1. (b) Horn #1

(c) Horn #2. (d) Horn #2.

Fig. 13: Measured (a,c) co- and (b,d) cross-polarization patterns versus the frequency and the polar angle θ along the H-plane.

The frequency stability of the beam direction can be observed from Fig. 13, where the normalized co- and cross-polarization are reported as a function of the polar angle θ

This article has been accepted for publication in a future issue of this journal, but has not been fully edited. Content may change prior to final publication. Citation information: DOI 10.1109/TAP.2022.3142369, IEEE Transactions on Antennas and Propagation

TABLE I: STATE-OF-THE-ART COMPARISON OF LINEARLY-POLARIZED CONTINUOUS TRANSVERSE STUB ARRAYS

Ref.	Fabrication technology	Freq. (GHz)	Relative bandwidth (%)	Thickness (λ_0)	No. stubs	No. layers	First SLLs (dB)	Scan range (°)
[29]	n.a.	31.5	20	0.16	18	2	E-plane: -5 H-plane: -20	-43 to 3 (E-plane)
[4]	CNC milling	29	12	4.3	16	n.a.	E-plane: -13 H-plane: -30	± 40 (H-plane)
[30]	CNC milling + PCB	78.5	11	8.8	32	n.a.	E-plane: -13.3 H-plane: -21	No scan
[31]	CNC milling	15.5	n.a.	n.a.	16	8	H-plane: -15.6	± 30 (H-plane)
[7]	LTCC	60	25.2	0.9	4	18	H-plane: -17.5 E-plane: -13.5	No scan
[32]	PCB	30	3	0.45	16	3	n.a.	No scan
[33]	CNC milling	33	42.4	2.8	16	5	E-plane: -13.3 H-plane: -12.1	No scan
[34]	CNC milling	37.5	18.7	2.5	8	4	E-plane: -13 H-plane: -13	No scan
[35]	PCB	27	18.2	0.53	8	4	E-plane: -13 H-plane: -13.5	No scan
[36]	PCB	20.5	32.6	0.53	8	6	E-plane: -13 H-plane: -13	No scan
[37]	PCB	15	30	0.3	8	3	H-plane: -25.2	± 35 (E-plane)
[38]	CNC milling	80	25	2.9	32	4	E-plane: -25.5 H-plane: -25.5	No scan
[8]	PCB	78.5	19	0.78	16	11	E-plane: -12 H-plane: -18	No scan
This work	PCB	25	50	0.5	8	9	E-plane: -15 H-plane: -25	± 22.5 (H-plane)

* λ_0 is the free-space wavelength at the reference frequency.

TABLE II: POWER BUDGET OF THE ANTENNA MODULE

Freq. (GHz)	Directivity (dBi)	Real. gain (dBi)	Efficiency (%)	Estimated ILs (dB)			Estimated mismatch losses (dB)
19	19.4	16.5	50.9	Transition 0.40	Pillbox 0.64	CFN 1.44	0.45
25	21.8	18.1	42.5	Transition 0.40	Pillbox 0.74	CFN 2.13	0.45
31	23.6	19.7	39.9	Transition 0.40	Pillbox 0.77	CFN 2.32	0.45

* The measured results refer to horn #1 excitation, i.e., broadside radiation.

(along the H-plane) and frequency. Specifically, the broadside beam [see Fig. 13(a)] is very stable in terms of pointing angle and half power beam-width over the 19-31 GHz band. On the contrary, a slight beam squint is observed at low frequencies for horn #2 excitation, as shown in Fig. 13(c). This effect is likely due to variations of the field tapering on the parabola profile and/or the fact that the focal distance of the parabola varies significantly at those frequencies, thus providing a different phase distribution along the radiating stubs. This pointing variation is predicted by simulations (not reported here for the sake of brevity) and deemed negligible. Furthermore, the cross-polarization, normalized to the peak value of the co-polarization, is plotted in Figs. 13(b) and (d) for horn #1 and #2, respectively. The measured results show that the cross-polarization discrimination (XPD) is below 25 dB everywhere in the 19-31 GHz frequency range.

For broadside radiation, the realized gain ranges from 16.5 to 19 dBi within the 19-31 GHz band, whereas the measured radiation efficiency is between 40% and 51%. The radiation efficiency is confirmed by full-wave simulations with estimated ILs on the order of 3 dB. A power budget is reported in Table II for the various blocks of which the antenna is composed.

A. State-of-the-art comparison of CTS arrays

Here, the performance and technical details of the antenna array proposed in this paper are compared with the state-of-the-art CTS arrays. Table I lists the major contributions that have been published in the last decade. Different types of CTS arrays can be found in open literature. For the case of slots fed in parallel, the feeding system may be a quasi-optical beamformer (e.g., pillbox coupler [4], [7], [8], [30] or others [36]), a ridged waveguide [31] or a generic linear source generator [32]–[34], [38].

The configuration employing a quasi-optical beamformer as a feeding system definitely stands out as optimal in terms of performance (e.g., wideband operation, large field-of-views, etc.). The antenna proposed in this paper is appealing as it achieves an ultra-low-profile (about half a free-space wavelength at the central frequency). Also, the operational bandwidth is about 50%: the largest achieved to date by a CTS array. The scan range is about $\pm 22.5°$ in elevation and can be further enlarged by displacing more horns along the focal plane of the parabola.

The solutions proposed in [32]–[34], [38] use a linear source generator as a feeding system. They can also achieve broadband operation (up to 42.4% [33]). On the other hand, these solutions are limited to fixed boresight beam radiation only.

Finally, CTS arrays can also be series-fed. In Table I, papers [29], [37] propose two designs for this class of anten-

This article has been accepted for publication in a future issue of this journal, but has not been fully edited. Content may change prior to final publication. Citation information: DOI 10.1109/TAP.2022.3142369, IEEE Transactions on Antennas and Propagation

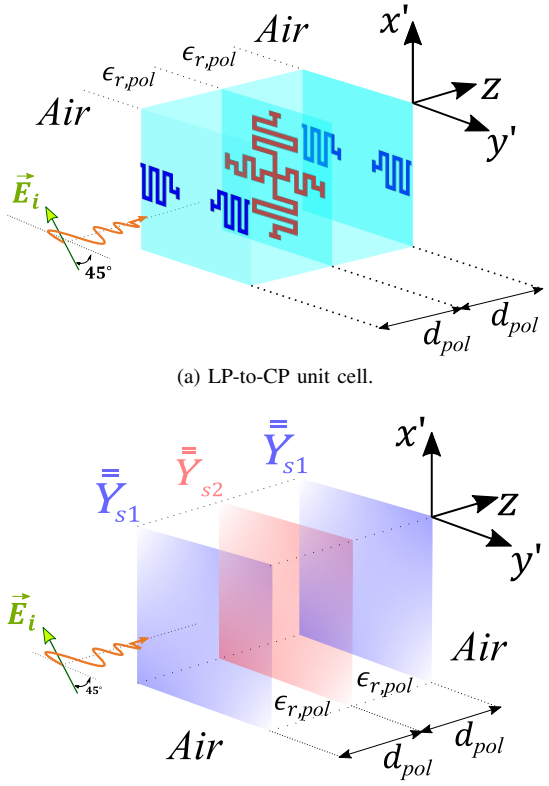

(a) LP-to-CP unit cell.

(b) Approximated model.

Fig. 14: (a) Unit cell of the LP-to-CP converter. (b) Equivalent model based on admittance boundary conditions. Simulations are carried out in periodic environment considering $d_{pol} = 1.524$ mm, $\epsilon_{r,pol} = 3$, and $\mathbf{E_i} = E_{i,x}\hat{x}$.

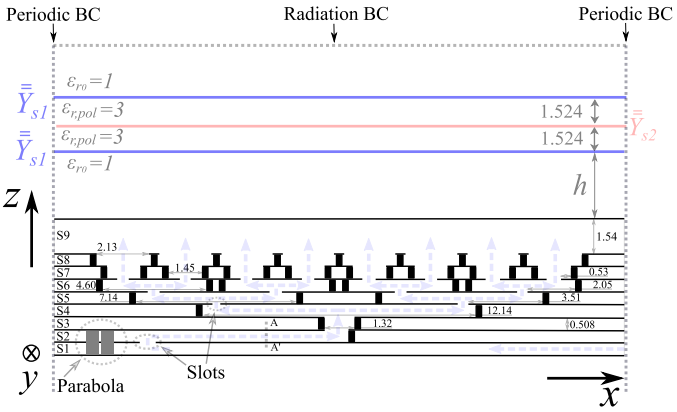

(a) Simulation setup.

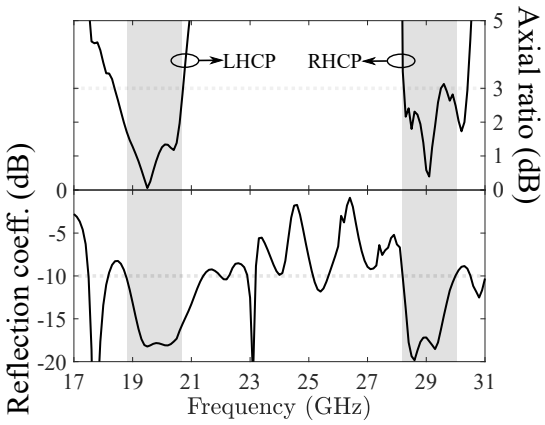

(b) Simulated results.

Fig. 15: (a) Simulation setup. (b) Simulated axial ratio (AR) and reflection coefficient (at cross-section AA') for $h = 70$ mm. The main beam points at broadside. All dimensions are in millimeters.

nas. Among their main advantages is its ultra-thin thickness. However, the pointing angle of the antenna array varies with frequency. The latter turns out to be problematic for point-to-point links which are recommended in high-throughput SatCom applications. The antenna proposed here overcomes this issue by attaining stable pointing angles across the operating band [see Fig. 13] while maintaining an ultra-low-profile design.

IV. CTS ARRAY WITH THE DUAL-BAND POLARIZER

The aim of this section is to present the performance of the CTS array, when combined with the dual-band linear-to-circular polarization (LP-to-CP) converter presented in [17]. The LP-to-CP converter is used as add-on component and placed above the antenna aperture. The overall system radiates orthogonal CPs over two non-adjacent frequency bands.

A. Equivalent model using admittance boundary conditions

The LP-to-CP converter is made of three bianisotropic metasurfaces realized as a periodic array of metallic textures and fabricated in multi-layer PCB technology. The metasurfaces' unit cells are shown in Fig. 14(a). The simulation setup considers an x-polarized plane wave, i.e., $\mathbf{E_i} = E_{i,x}\hat{x}$, impinging onto the polarizer's unit cell. The latter is arranged into a 2-D periodic lattice and thus simulated using periodic boundary conditions. The polarizer prototype has been fabricated in multi-layer PCB technology using two Rogers RO3003^{TM} substrates [25] glued together with Taconic FastRise^{TM} FR-27-0030-25 (F). Further details and all geometrical dimensions can be found in [17].

The combination of the CTS array with the LP-to-CP converter constites an electrically-large structure that requires an elevated computational cost to be simulated. For this reason, the physical unit cells in Fig. 14(a) are approximated as sheet admittances as shown in Fig. 14(b). Each sheet admittance is bianisotropic and it is modeled using equivalent circuit models as done in [17]. This approximated model reduces complexity and enables to run parametric analyses to retrieve the optimal polarizer position over the CTS array. More specifically, the cross-sectional view of the simulation setup CTS array plus polarizer's approximated model) is shown in Fig. 15(a). The CFN of the array is simulated in a periodic environment using HFSS [27], as shown in Fig. 5. Three sheet admittances are placed on top of the radiating aperture at distance h. Two consecutive sheets are separated by a dielectric slab of dielectric constant $\epsilon_{r,pol} = 3$ and thickness 1.524 mm. The structure is excited from section AA' using a TEM wave. The electric sheet admittances are anisotropic and their tensors are

This article has been accepted for publication in a future issue of this journal, but has not been fully edited. Content may change prior to final publication. Citation information: DOI 10.1109/TAP.2022.3142369, IEEE Transactions on Antennas and Propagation

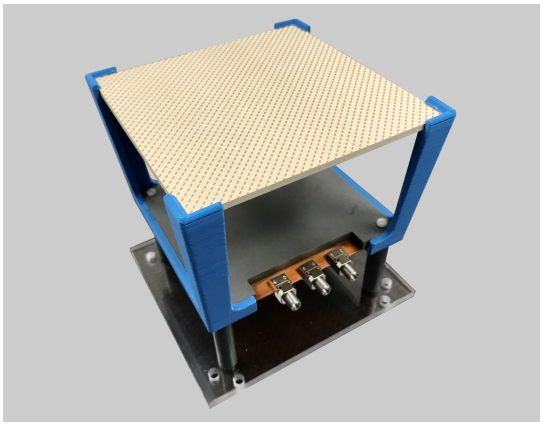

Fig. 16: Photograph of the prototype: CTS array combined with dual-band LP-to-CP converter.

given by

$$\bar{\bar{Y}}_{s1} = \begin{bmatrix} \left(i\omega L_{s1}^{x'x'}\right)^{-1} & 0 \\ 0 & \left(i\omega L_{s1}^{y'y'} + \frac{1}{i\omega C_{s1}^{y'y'}}\right)^{-1} \end{bmatrix} \quad (1)$$

$$\bar{\bar{Y}}_{s2} = \begin{bmatrix} \left(i\omega L_{s2}^{x'x'} + \frac{1}{i\omega C_{s2}^{x'x'}}\right)^{-1} & 0 \\ 0 & \left(i\omega L_{s2}^{y'y'} + \frac{1}{i\omega C_{s2}^{y'y'}}\right)^{-1} \end{bmatrix} \quad (2)$$

where ω is the angular frequency and the lumped element values $L_{s1}^{x'x'}$, $L_{s1}^{y'y'}$, $C_{s1}^{y'y'}$, $L_{s2}^{x'x'}$, $C_{s2}^{x'x'}$, $L_{s2}^{y'y'}$, and $C_{s2}^{y'y'}$ can be found in [17]. The entries of $\bar{\bar{Y}}_{s1}$ and $\bar{\bar{Y}}_{s2}$ refer to a Cartesian reference system (x', y') which is rotated by 45° with respect to the x-axis depicted in Fig. 15(a). The impinging field $\mathbf{E_i}$ in Fig. 14 is here replaced by the x-polarized fields radiated by the CTS array. The distance h is optimized by means of a parametric study. The optimum is found for $h = 70$ mm. Note that such a distance can be further optimized through a co-design of the CTS array and the polarizer. The simulated axial ratio (AR) and reflection coefficient (at section AA') are reported in Fig. 15(b). The grey areas in Fig. 15(b) indicate the bands of operation. They are defined as the frequency ranges for which $AR < 3$ dB and the reflection coefficient is below -10 dB. As shown in Fig. 15(b), the antenna system radiates LHCP within the 18.7-20.7 GHz frequency band and RHCP over the 28.2-30 GHz band. These simulated results are approximate since they do not refer to a real structure for the polarizer. However, they provide an estimate of the attainable performance of the structure. Note that the simulations in Fig. 15(b) refer to broadside radiation.

B. Prototype and measured results

As shown in Fig. 16, a plastic support has been fabricated to hold the polarizer at 70 mm above the radiating aperture. The measured radiation patterns are reported in Fig. 17. They are plotted in the (ξ, ζ) space. These two angles correspond to the elevation and azimuth angles used during measurements. Specifically, the angle ξ is the polar angle in the xz-plane for a given direction in the yz-plane [refer to Fig. 1]. For instance, the scanning plane (yz-plane) is associated with the portion of the (ξ, ζ) space corresponding to $\zeta = 0°$. The measured patterns shown in Fig. 17 are normalized to the peak value of the co-polar radiated component. They have been carried out by performing measurements in the anechoic chamber at 21.5 GHz [see Figs. 17(a)-to-(f)] and 29 GHz [see Figs. 17(g)-to-(l)]. These two frequencies are chosen as references to demonstrate that orthogonal CPs are radiated in the down- and up-link channels of K/Ka-band SatComs. Indeed, the antenna system in Fig. 16 radiates LHCP at low frequencies, as it can be oberserved from Figs. 17(a) and (b) at broadside and Figs. 17(d) and (e) when scanning. As shown in Figs. 17(b) and (e), the XPD is around 15 dB and 17 dB for horn #1 and #2 excitation, respectively. The XPD is slightly worse for horn #1 since multiple reflections may occur between the polarizer and the CTS array for broadside radiation. Furthermore, the polarization purity is characterized in terms of AR and is shown in Figs. 17(c) and (f). The latter shows that the AR is below 3 dB around the pointing direction of the array for absolute polar ranges larger than 10°. Therefore, the AR is satisfactory stable around the main beam direction.

The measured patterns in the upper band are shown in Figs. 17(g)-to-(l). In this case, the co-polar radiated component is measured to be the RHCP at 29 GHz. By comparing Fig. 17(g) with Fig. 17(h) and Fig. 17(j) with Fig. 17(k), the XPD is about 19 dB for both horns #1 and #2. The AR patterns at 29 GHz are plotted in Figs. 17(i) and (l) for horn #1 and #2 excitation, respectively. The latter is lower than 3 dB around the pointing angle of the array within a field-of-view of about ±15° in elevation.

For the sake of completeness, the AR at the pointing angle is plotted in Fig. 18 versus frequency. The measurements are compared with those for the LP-to-CP converter as self-standing device (dashed red curve in Figs. 18(a) and (b)) as reported in [17]. The measurements are in a good agreement with those of the stand-alone polarizer, although small differences can be attributed to multiple reflections between the polarizer and antenna aperture. Specifically, the AR is below 3 dB within the frequency band 20.1-22.1 GHz (9.47% relative bandwidth) for broadside radiation. The performance is also much stable in scanning. On the other hand, Fig. 18(b) plots the measured AR at high frequencies. Within the up-link channel, the antenna system performs with an AR below 3 dB over the frequency band 28.7-30 GHz (4.42% relative bandwidth).

C. State-of-the-art dual-band, dual-circular-polarized antennas

Table III summarizes the state-of-the-art for dual-band antennas with orthogonal CP radiation at two separate operating bands. Patch arrays propose a solution to these requirements. The geometries of these radiators can be annular ring slots [39] or square patches with rotated rectangular slots etched into them [40]. However, these antennas do not perform scan. Scanning performance can be achieved by relying on phased array modules. As a drawback, the latter solution is significantly power consuming.

This article has been accepted for publication in a future issue of this journal, but has not been fully edited. Content may change prior to final publication. Citation information: DOI 10.1109/TAP.2022.3142369, IEEE Transactions on Antennas and Propagation

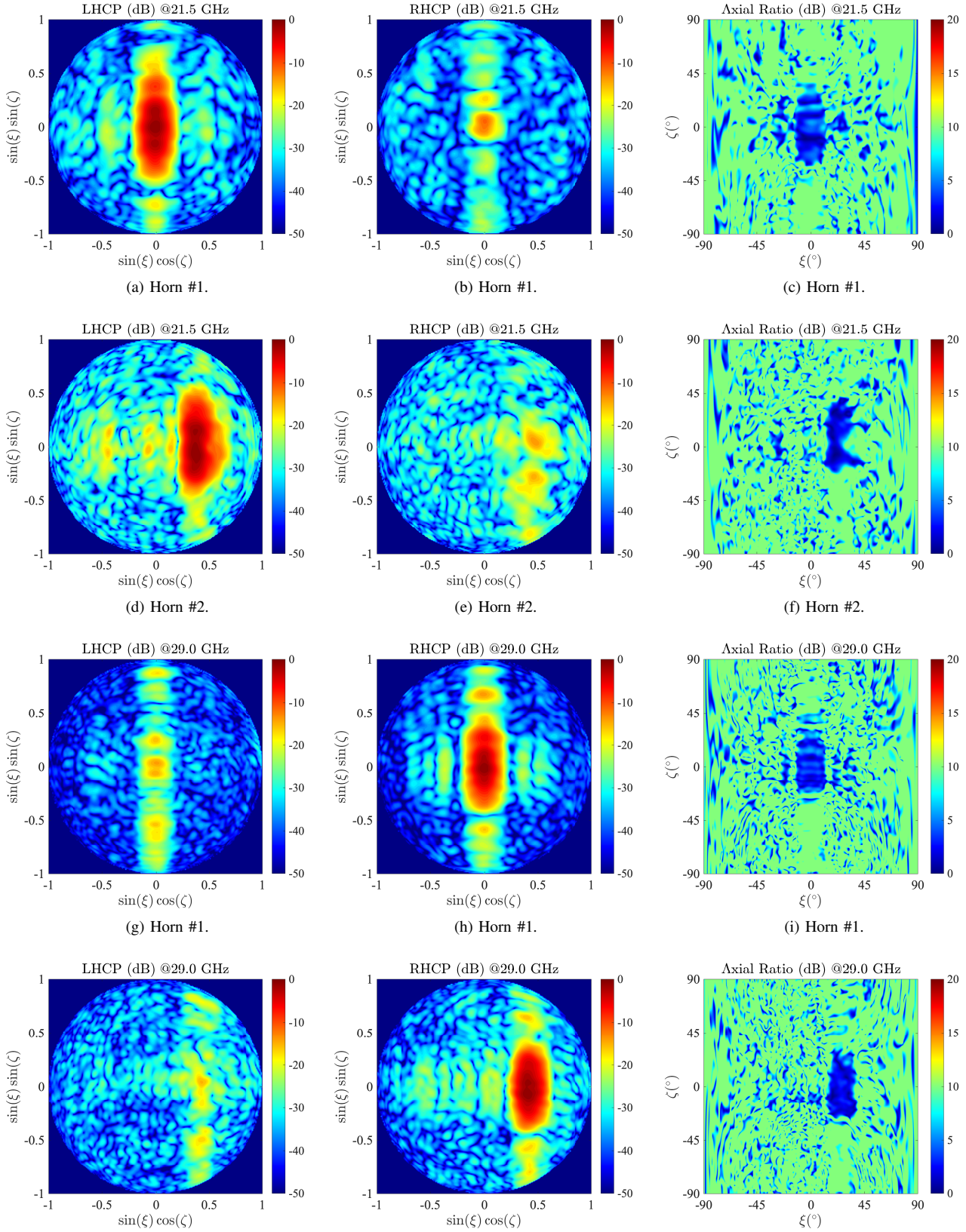

(a) Horn #1. (b) Horn #1. (c) Horn #1.

(d) Horn #2. (e) Horn #2. (f) Horn #2.

(g) Horn #1. (h) Horn #1. (i) Horn #1.

(j) Horn #2. (k) Horn #2. (l) Horn #2.

Fig. 17: Measured normalized patterns at 21.5 and 29 GHz. (a), (d), (g), and (j) LHCP patterns. (b), (e), (h), and (k) RHCP patterns. (c), (f), (i), and (l) axial ratio patterns.

This article has been accepted for publication in a future issue of this journal, but has not been fully edited. Content may change prior to final publication. Citation information: DOI 10.1109/TAP.2022.3142369, IEEE Transactions on Antennas and Propagation

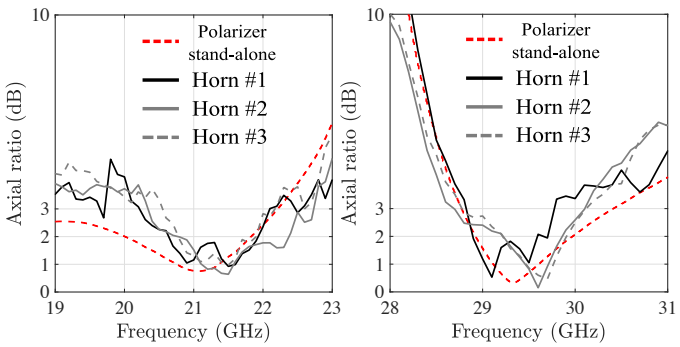

(a) Down-link. (b) Up-link.

Fig. 18: Measured axial ratio of the prototype shown in Fig. 16. The axial ratio is reported as a function of frequency. It is calculated in the pointing direction of the array. (a) Up- and (b) down-link.

TABLE III: STATE-OF-THE-ART COMPARISON OF DUAL-BAND, ORTHOGONALLY POLARIZED ANTENNAS

Ref.	Type	Freq. (GHz)	Relative bandwidth (%)	Scan range (°)
[39]	Patch array	20 and 30	10 and 6.6	No scan
[40]	Patch array	12 and 17	12 and 17	No scan
[41]	Patch array	2.52 and 3.57	0.4 and 0.28	No scan
This work	CTS array + polarizer	21.5 and 29.5	9.47 and 4.42	± 22.5 (yz-plane)

* The relative bandwidth is the frequency range for which $AR < 3$ dB.

For the first time, this paper introduces a hybrid solution based on a very wideband antenna array used in combination with a metasurface-based, dual-band LP-to-CP converter. The proposed architecture attains dual-circular polarization within the K/Ka-band up- and down-links by resorting to a single low-profile device. This solution has to be optimized to lower the profile of the overall module (CTS array combined with the polarizer). On the other hand, it represents an important proof-of-concept of high performing ground terminals for next generation SatCom applications.

V. CONCLUSION

The design of an ultra-low-profile continuous transverse stub array has been introduced in this paper. The antenna is fully realized in multi-layer printed circuit board technology by employing 9 dielectric substrates. The antenna height is about half a wavelength at the central frequency. The array maintains linear polarization over the band 19-31 GHz (48% fractional bandwidth). Measurements validate the design. Specifically, the antenna attains cross polar discrimination up to 25 dB and very stable pointing angles are observed in the full operating band. Beam steering is enabled along the H-plane for polar angles as far as $\pm 22.5°$. The scanning performance is attained by means of a quasi-optical system, embedded into two stacked substrates. The overall antenna module is then combined with a dual-band, orthogonally-polarized linear-to-circular polarization converter proposed in [17]. The latter provides orthogonal circular polarization between the down- and the up-links of modern K/Ka-band satellite communications. The polarized converts the linear polarized waves radiated by the continuous transverse stub array into dual-circular polarized fields. The overall antenna system shows an axial ratio below 3 dB for left-hand circular polarized radiation within the band 20.1-22.1 GHz. A similar performance is achieved in the 28.7-30 GHz band for right-hand circular polarization. The proposed antenna array is a promising candidate for next generation satellite communication terminals that can operate in both receive and transmit channels of K/Ka-band by resorting to a single radiating aperture.

ACKNOWLEDGMENT

This work was partly supported by ANR-ASTRID MATURATION (project named RAFQO) and by Thales SIX GTS France. This work was also supported by the European Union through the European Regional Development Fund (ERDF), and also by Ministry of Higher Education and Research, Brittany and Rennes Métropole, through the CPER Project SOPHIE/STIC & Ondes.

The authors would also like to thank Dr. Laurent Le Coq for his help in performing the measurements.

REFERENCES

[1] B.R. Rao, K. McDonald, and W. Kunysz. *GPS/GNSS Antennas*. Artech House telecommunications library. Artech House, 2013. isbn: 9781596931503.

[2] R. A. Pearson, J. Vazquez, M. W. Shelley, A. Payne, V. Stoiljkovic, and M. Steel, "Next generation mobile SATCOM terminal antennas for a transformed world," *Proc. 5^{th} Eur. Conf. Antennas Propag. (EUCAP)*, Rome, Italy, 2011, pp. 2341–2345.

[3] T. Rossi, M. De Sanctis, M. Ruggieri, C. Riva, L. Luini, G; Codispoti, E. Russo, and G. Parca, "Satellite communication and propagation experiments through the alphasat Q/V band Aldo Paraboni technology demonstration payload," *IEEE Aerospace Electronic Systems Magazine*, vol. 31, no. 3, pp. 18-27, Mar. 2016, doi: 10.1109/MAES.2016.150220.

[4] M. Ettorre, F. F. Manzillo, M. Casaletti, R. Sauleau, L. Le Coq and N. Capet, "Continuous transverse stub array for Ka-band applications," *IEEE Trans. Antennas Propag.*, vol. 63, no. 11, pp. 4792-4800, Nov. 2015, doi: 10.1109/TAP.2015.2479243.

[5] R. Sauleau and M. Ettorre, "Multilayer pillbox type parallelplate waveguide antenna and corresponding antenna system," U.S. Patent 9 246 232, Jan. 26, 2016

[6] M. Ettorre, R. Sauleau and L. Le Coq, "Multi-beam multi-layer leaky-wave SIW pillbox antenna for millimeter-wave applications," *IEEE Trans. Antennas Propag.*, vol. 59, no. 4, pp. 1093-1100, April 2011, doi: 10.1109/TAP.2011.2109695.

[7] F. Foglia Manzillo, M. Ettorre, M. S. Lahti, K. T. Lelaidier, E. Seguenot, and R. Sauleau, "A multilayer LTCC solution for integrating 5G access point antenna modules," *IEEE Trans. Microw. Theory Techn.*, vol. 64, no. 7, pp. 2272-2283, July 2016, doi: 10.1109/TMTT.2016.2574313.

[8] T. Potelon, M. Ettorre, L. Le Coq, T. Bateman, J. Francey and R. Sauleau, "Reconfigurable CTS antenna fully integrated in PCB technology for 5G backhaul applications," *IEEE Trans. Antennas Propag.*, vol. 67, no. 6, pp. 3609-3618, June 2019, doi: 10.1109/TAP.2019.2902644.

[9] M. Del Mastro, F. F. Manzillo, D. González-Ovejero, M. Śmierzchalski, P. Pouliguen, P. Potier, R. Sauleau, and M. Ettorre, "Analysis of circularly polarized CTS arrays," *IEEE Trans. Antennas Propag.*, vol. 68, no. 6, pp. 4571-4582, June 2020, doi: 10.1109/TAP.2020.2972438.

[10] S. Lenzini, M. Del Mastro, L. Vincetti and M. Ettorre, "Circularly-polarized CTS array antenna for SatCom applications," *2020 International Symposium on Antennas and Propagation (ISAP)*, 2021, pp. 591-592, doi: 10.23919/ISAP47053.2021.9391326.

[11] M. Del Mastro, S. Lenzini, R. Sauleau and M. Ettorre, "Equidispersive dual-mode long slot arrays," *IEEE Antennas Wireless Popag. Lett.*, vol. 19, no. 12, pp. 2127-2131, Dec. 2020, doi: 10.1109/LAWP.2020.3024618.

[12] M. Śmierzchalski, F. F. Manzillo, M. Del Mastro, N. Capet, B. Palacin, R. Sauleau, and M. Ettorre, "A novel dual-polarized continuous transverse stub antenna based on corrugated waveguides—part I: principle of operation and design," *IEEE Trans. Antennas Propag.*, vol. 69, no. 3, pp. 1302-1312, March 2021, doi: 10.1109/TAP.2020.3028236.

[13] M. Śmierzchalski, F. F. Manzillo, M. Del Mastro, N. Capet, B. Palacin, R. Sauleau, and M. Ettorre, "A novel dual-polarized continuous transverse stub antenna based on corrugated waveguides—part II: experimental demonstration," *IEEE Trans. Antennas Propag.*, vol. 69, no. 3, pp. 1313-1323, March 2021, doi: 10.1109/TAP.2020.3037809.

[14] M. Del Mastro, A. Mahmoud, T. Potelon, R. Sauleau, G. Quagliaro and M. Ettorre, "Low-profile CTS array in PCB technology for K/Ka-band applications," *15^{th} Eur. Conf. Antennas Propag. (EUCAP)*, 2021, pp. 1-3, doi: 10.23919/EuCAP51087.2021.9411222.

[15] P. Naseri, S. A. Matos, J. R. Costa, C. A. Fernandes, and N. J. G. Fonseca, "Dual-band dual-linear-to-circular polarization converter in transmission mode application to K/Ka-band satellite communications," *IEEE Trans. Antennas Propag.*, vol. 66, no. 12, pp. 7128-7137, Dec. 2018, doi: 10.1109/TAP.2018.2874680.

[16] H. B. Wang, and Y. J. Cheng, "Single-layer dual-band linear-to-circular polarization converter with wide axial ratio bandwidth and different polarization modes," *IEEE Trans. Antennas Propag.*, vol. 67, no. 6, pp. 4296-4301, Jun. 2019, doi: 10.1109/TAP.2019.2905962.

[17] M. Del Mastro, M. Ettorre and A. Grbic, "Dual-band, orthogonally-polarized LP-to-CP converter for SatCom applications," *IEEE Trans. Antennas Propag.*, vol. 68, no. 9, pp. 6764-6776, Sept. 2020, doi: 10.1109/TAP.2020.2989868.

[18] N. Capet, F. Foglia Manzillo, K. Tekkouk, R. Sauleau, and M. Ettorre, "Multilayer waveguide comprising at least one transition device between layers of this multilayer waveguide," U.S. Patent 9 246 232, Jan. 26, 2016

[19] J. Ruiz-García, E. Martini, C. D. Giovampaola, D. González-Ovejero and S. Maci, "Reflecting Luneburg lenses," *IEEE Trans. Antennas Propag.*, doi: 10.1109/TAP.2020.3044668.

[20] J. E. Rayas-Sanchez and V. Gutierrez-Ayala, "A general EM-based design procedure for single-layer substrate integrated waveguide interconnects with microstrip transitions," *IEEE MTT-S International Microwave Symposium Digest*, Atlanta, GA, USA, 2008, pp. 983-986, doi: 10.1109/MWSYM.2008.4632999.

[21] D. Deslandes and K. Wu, "Design consideration and performance analysis of substrate integrated waveguide components," *32^{nd} European Microwave Conference*, Milan, Italy, 2002, pp. 1-4, doi: 10.1109/EUMA.2002.339426.

[22] Y. Cassivi, L. Perregrini, P. Arcioni, M. Bressan, K. Wu and G. Conciauro, "Dispersion characteristics of substrate integrated rectangular waveguide," *IEEE Microwave Wireless Comp. Lett.*, vol. 12, no. 9, pp. 333-335, Sept. 2002, doi: 10.1109/LMWC.2002.803188.

[23] Feng Xu and Ke Wu, "Guided-wave and leakage characteristics of substrate integrated waveguide," *IEEE Trans. Microw. Theory Techn.*, vol. 53, no. 1, pp. 66-73, Jan. 2005, doi: 10.1109/TMTT.2004.839303.

[24] Ke Wu, D. Deslandes and Y. Cassivi, "The substrate integrated circuits - a new concept for high-frequency electronics and optoelectronics," *6th International Conference on Telecommunications in Modern Satellite*, Cable and Broadcasting Service, 2003. TELSIKS 2003., Nis, Yugoslavia, 2003, pp. P-III, doi: 10.1109/TELSKS.2003.1246173.

[25] Rogers Corporation, https://www.rogerscorp.com

[26] Computer simulation technology, CST STUDIO SUITE, 2017.

[27] ANSYS Electronics Desktop 2018.2, High-Freq. Struct. Simul., Canonsburg, PA, USA, 2018

[28] E. Magill and H. Wheeler, "Wide-angle impedance matching of a planar array antenna by a dielectric sheet," *IEEE Trans. Antennas Propag.*, vol. 14, no. 1, pp. 49-53, Jan. 1966, doi: 10.1109/TAP.1966.1138622.

[29] H. Choe and S. Lim, "Millimeter-wave continuous transverse stub (CTS) antenna array using substrate integrated waveguide (SIW) technology," *IEEE Trans. Antennas Propag.*, vol. 62, no. 11, pp. 5497-5503, Nov. 2014, doi: 10.1109/TAP.2014.2347412.

[30] T. Potelon, M. Ettorre, L. Le Coq, T. Bateman, J. Francey, D. Lelaidier, E. Seguenot, F. Devillers, and R. Sauleau, "A low-profile broadband 32-slot continuous transverse stub array for backhaul applications in E-band," *IEEE Trans. Antennas Propag.*, vol. 65, no. 12, pp. 6307-6316, Dec. 2017, doi: 10.1109/TAP.2017.2712791.

[31] X. Lu, S. Gu, X. Wang, H. Liu and W. Lu, "Beam-scanning continuous transverse stub antenna fed by a ridged waveguide slot array," *IEEE Antennas Wireless Popag. Lett.*, vol. 16, pp. 1675-1678, 2017, doi: 10.1109/LAWP.2017.2664880.

[32] X. L. Liu and Y. J. Cheng, "Planar parallel-plate waveguide continuous transverse stub antenna array fed by substrate integrated waveguide divider," *IEEE 4th Asia-Pacific Conf. Antennas Propag.*, Bali, Indonesia, 2015, pp. 283-284, doi: 10.1109/APCAP.2015.7374374.

[33] Q. You, Y. Lu, Y. You, Y. Wang, Z. Hao and J. Huang, "Wideband full-corporate-feed waveguide continuous transverse stub antenna array," *IEEE Access*, vol. 6, pp. 76673-76681, 2018, doi: 10.1109/ACCESS.2018.2883590.

[34] Q. C. You, Y. L. Lu, G. M. Xu and J. F. Huang, "Design of a 4 × 4 low profile continuous transverse stub antenna array," *Progress Electromagnetics Research Symposium - Fall (PIERS - FALL)*, Singapore, 2017, pp. 1465-1469, doi: 10.1109/PIERS-FALL.2017.8293362.

[35] Y. Lu, Q. You, Y. Wang, Y. You, J. Huang and K. Wu, "Millimeter-wave low-profile continuous transverse stub arrays with novel linear source generators," *IEEE Trans. Antennas Propag.*, vol. 67, no. 2, pp. 988-997, Feb. 2019, doi: 10.1109/TAP.2018.2883574.

[36] Y. Gao, T. Hong, W. Jiang, S. Gong and F. Li, "Low-profile wideband CTS array using substrate-integrated waveguide technology for K-band applications," *IEEE Trans. Antennas Propag.*, vol. 67, no. 8, pp. 5711-5716, Aug. 2019, doi: 10.1109/TAP.2019.2916653.

[37] H. Qiu, X. Yang, Y. Yu, T. Lou, Z. Yin and S. Gao, "Compact beam-scanning flat array based on substrate-integrated waveguide," *IEEE Trans. Antennas Propag.*, vol. 68, no. 2, pp. 882-890, Feb. 2020, doi: 10.1109/TAP.2019.2943441.

[38] Y. You, Y. Lu, Y. Wang, W.-W. Yang, Z.-C. Hao, Q. You, and J. Huang, "High-performance E-band continuous transverse stub array antenna with a 45° linear polarizer," *IEEE Antennas Wireless Popag. Lett.*, vol. 18, no. 10, pp. 2189-2193, Oct. 2019, doi: 10.1109/LAWP.2019.2940127.

[39] S. Mener, R. Gillard and L. Roy, "A dual-band dual-circular-polarization antenna for Ka-band satellite communications," *IEEE Antennas Wireless Popag. Lett.*, vol. 16, pp. 274-277, 2017, doi: 10.1109/LAWP.2016.2572261.

[40] J. Zhang, W. Wu and D. Fang, "Dual-band and dual-circularly polarized shared-aperture array antennas with single-layer substrate," *IEEE Trans. Antennas Propag.*, vol. 64, no. 1, pp. 109-116, Jan. 2016, doi: 10.1109/TAP.2015.2501847.

[41] J. Zhang, L. Zhu, N. Liu and W. Wu, "Dual-band and dual-circularly polarized single-layer microstrip array based on multi-resonant modes," *IEEE Trans. Antennas Propag.*, vol. 65, no. 3, pp. 1428-1433, Mar. 2017, doi: 10.1109/TAP.2016.2647582.

[42] Southwest Microwave Inc.: https:// mpd.southwestmicrowave.com.

This article has been accepted for publication in a future issue of this journal, but has not been fully edited. Content may change prior to final publication. Citation information: DOI 10.1109/TAP.2022.3142369, IEEE Transactions on Antennas and Propagation

Michele Del Mastro was born in Avellino, Italy, on July 25^{th}, 1992. He received the M. Mus. degree in clarinet from the Conservatorio di Musica 'D. Cimarosa', Avellino, Italy, in 2011, and the M.Sc. degree (*summa cum laude*) in electronics engineering from the Università degli Studi di Napoli 'Federico II', Naples, Italy, in 2017. He also obtained the Ph.D. degree in electrical engineering from the Institut d'Électronique et des Technologies du numéRique (IETR), Université de Rennes 1, Rennes, France, in 2020.

In 2016, he joined the Electronic Research Laboratory, Delft University of Technology, Delft, The Netherlands, as an intern. From May to October 2019, he was Visiting Ph.D. Scholar with the Radiation Laboratory, University of Michigan, Ann Arbor, MI, USA, where he developed part of his Ph.D. work. He is currently serving as an Antenna Engineer with Anywaves, Toulouse, France, involved in Research and Development activities on innovative antenna solutions for LEO satellite constellations.

His research interests include the analysis and synthesis of wideband antenna arrays, numerical modeling, metasurface-based polarization converters, and miniaturized antenna solutions for satellite telemetry/telecommand.

Dr. Del Mastro was the recipient of a Doctoral Award issued by Fondation Rennes 1, a non-profit organization that aims at promoting progress, innovation and entrepreneurship. He also received the Best Antennas Paper Award at 15^{th} European Conference on Antennas and Progagation (EuCAP), Düsseldorf, Germany, in 2021. Furthermore, Dr. Del Mastro was a co-recipient of the Innovation Award at the 39^{th} European Space Agency Antenna Workshop, Noordwijk, The Netherlands, in 2018, and received the TICRA Foundation Travel Grant at the 13^{th} European Conference on Antennas and Propagation (EuCAP), Krakow, Poland, in 2019.

Adham Mahmoud was born in 1993. He received the master's degree in communication engineering from the German university in Cairo, Cairo, Egypt, in 2016, and the Ph.D. degree in electrical engineering from the University of Rennes 1, Rennes, France, in 2021. Currently, he is working as a CNRS Post-Doctoral Researcher with the Institut d'Électronique et des Technologies du numéRique (IETR), Rennes. His research interests include the design of millimeter and sub-millimeter wave antenna arrays, slotted waveguide antenna arrays, high-gain antennas and ultra wideband antennas.

Thomas Potelon was born in 1991. He received the master's degree in electronic and numerical technologies from the École Polytechnique de l'Université de Nantes, Nantes, France, in 2014, and the Ph.D. degree in electrical engineering from the University of Rennes 1, Rennes, France, in 2017. He then worked for 2 years as a CNRS Post-Doctoral Researcher with the Institut d'Électronique et des Technologies du numéRique (IETR), Rennes. His research interests included the analysis and design of millimeter-wave antennas, high-gain antennas, and reconfigurable antennas. Since 2020, he works for the Ministry of Armed Forces (France) as a radio frequency engineer.

Ronan Sauleau (M'04–SM'06–F'18) graduated in electrical engineering and radio communications from the Institut National des Sciences Appliquées, Rennes, France, in 1995. He received the Agrégation degree from the Ecole Normale Supérieure de Cachan, France, in 1996, and the Doctoral degree in signal processing and telecommunications and the "Habilitation à Diriger des Recherches" degree, both from the University of Rennes 1, France, in 1999 and 2005, respectively.

He was an Assistant Professor and Associate Professor at the University of Rennes 1, between September 2000 and November 2005, and between December 2005 and October 2009, respectively. He has been appointed as a full Professor in the same University since November 2009. His current research fields are numerical modeling, millimeter-wave printed and reconfigurable (MEMS) antennas, substrate integrated waveguide antennas, lens-based focusing devices, periodic and non-periodic structures (electromagnetic bandgap materials, metamaterials, reflectarrays, and transmitarrays) and biological effects of millimeter waves. He has been involved in more than 70 research projects at the national and European levels and has co-supervised 27 post-doctoral fellows, 53 PhD students and 50 master students.

He has received 20 patents and is the author or coauthor of more than 270 journal papers and 560 publications in international conferences and workshops. He has shared the responsibility of the research activities on antennas at IETR in 2010 and 2011. He was co-director of the research Department 'Antenna and Microwave Devices' at IETR and deputy director of IETR between 2012 and 2016. He is now director of IETR. Prof. Sauleau received the 2004 ISAP Conference Young Researcher Scientist Fellowship (Japan) and the first Young Researcher Prize in Brittany, France, in 2001 for his research work on gain-enhanced Fabry-Perot antennas. In September 2007, he was elevated to Junior member of the "Institut Universitaire de France". He was awarded the Bronze medal by CNRS in 2008, and the silver medal in 2020. He received the 2021 Antenna EurAAP Award. He was the co-recipient of several international conference awards with some of his students (Int. Sch. of BioEM 2005, BEMS'2006, MRRS'2008, E-MRS'2011, BEMS'2011, IMS'2012, Antem'2012, BioEM'2015, EuCAP'2019, EuCAP'2021). He served as a guest editor for the IEEE Antennas Propogat. Special Issue on "Antennas and Propagation at mm and sub mm waves". He served as a national delegate for several EU COST actions. He has served as a national delegate for EurAAP and as a member of the board of Director of EurAAP from 2013 to 2018.

Gilles Quagliaro graduated from the Higher School of Electricity (Supelec, France) in 1980. He worked for several years at Thales and was involved in many radiocommunication projects. He is a recognized expert in space telecommunications, including aeronautical satcoms and flat panel antennas.

This article has been accepted for publication in a future issue of this journal, but has not been fully edited. Content may change prior to final publication. Citation information: DOI 10.1109/TAP.2022.3142369, IEEE Transactions on Antennas and Propagation

Anthony Grbic received the B.A.Sc., M.A.Sc., and Ph.D. degrees in electrical engineering from the University of Toronto, Canada, in 1998, 2000, and 2005, respectively. In 2006, he joined the Department of Electrical Engineering and Computer Science, University of Michigan, Ann Arbor, MI, USA, where he is currently a Professor. His research interests include engineered electromagnetic structures (metamaterials, metasurfaces, electromagnetic band-gap materials, frequency-selective surfaces), microwave circuits, antennas, plasmonics, wireless power transmission, and analytical electromagnetics/optics.

Anthony Grbic has made pioneering contributions to the theory and development of electromagnetic metamaterials and metasurfaces: finely textured, engineered electromagnetic structures/surfaces that offer unprecedented wavefront control. Dr. Grbic is a Fellow of the IEEE, and is currently an IEEE Microwave Theory and Techniques Society Distinguished Microwave Lecturer (2022-2025). He is also serving on the IEEE Antennas and Propagation Society (AP-S) Field Awards Committee and IEEE Fellow Selection Committee. From 2018 to 2021, he has served as a member of the Scientific Advisory Board, International Congress on Artificial Materials for Novel Wave Phenomena – Metamaterials. In addition, he has been Vice Chair of Technical Activities for the IEEE Antennas and Propagation Society, Chapter IV (Trident), IEEE Southeastern Michigan Section, from Sept. 2007 – 2021. From July 2010 to July 2015, he was Associate Editor for the rapid publication journal IEEE Antennas and Wireless Propagation Letters. Prof Grbic was Technical Program Co-Chair in 2012 and Topic Co-Chair in 2016 and 2017 for the IEEE International Symposium on Antennas and Propagation and USNC-URSI National Radio Science Meeting. Dr. Grbic was the recipient of AFOSR Young Investigator Award as well as NSF Faculty Early Career Development Award in 2008, the Presidential Early Career Award for Scientists and Engineers in January 2010. He also received an Outstanding Young Engineer Award from the IEEE Microwave Theory and Techniques Society, a Henry Russel Award from the University of Michigan, and a Booker Fellowship from the United States National Committee of the International Union of Radio Science in 2011. He was the inaugural recipient of the Ernest and Bettine Kuh Distinguished Faculty Scholar Award in the Department of Electrical and Computer Science, University of Michigan in 2012. In 2018, Prof. Anthony Grbic received a 2018 University of Michigan Faculty Recognition Award for outstanding achievement in scholarly research, excellence as a teacher, advisor and mentor, and distinguished service to the institution and profession. In 2021, he was selected as 1 of 5 finalists for the A.F. Harvey Engineering Research Prize, for his contributions to the field of electromagnetic metamaterials.

Mauro Ettorre (M'08–SM'15) received a Laurea degree "*summa cum laude*" in Electrical Engineering, and a Ph.D. degree in Electromagnetics from the University of Siena, Italy, in 2004 and 2008, respectively. Part of his Ph.D. work was developed at the Netherlands Organisation for Applied Scientific Research (TNO), The Hague, the Netherlands, where he later worked as an Antenna Researcher. From 2008 to 2010, Dr. Ettorre was a Postdoctoral Fellow at Institut d'Electronique et de Télécommunications de Rennes (IETR), University of Rennes 1, France. In 2010 and 2016, he was a Visiting Scholar in the Radiation Laboratory, Department of Electrical Engineering and Computer Science, University of Michigan, USA. Since October 2010, he is a Research Scientist at the Centre National de la Recherche Scientifique (CNRS), within the IETR. From 2014 until 2020, he assumed responsibilities for the multi-beam antenna activity for satellite applications in the joint laboratory between IETR and Thales Alenia Space, France. Since 2017, he serves as Associate Editor for the IEEE Transaction on Antennas and Propagation. In 2017, 2018, and 2019 he was member of the best paper award selection committee for the IEEE Transactions on Terahertz Science and Technology. In 2020, he co-founded the open access journal Reviews on Electromagnetics of European Association on Antennas and Propagation (EurAAP) for which he serves as Associate Editor. In 2020 and 2021 he was appointed EurAAP ambassador. In 2020 and 2021 he was appointed European Association on Antennas and Propagation (EurAAP) ambassador.

Dr. Ettorre's research interests include the analysis and design of leaky-wave antennas, periodic structures, millimeter-wave antennas, non-diffractive radiation and localized waves, near-field focusing techniques, and wireless power transfer systems.

Dr. Ettorre received the Young Antenna Engineer Prize at the 2008 ESA Antenna Workshop in the Netherlands, the Innovation Award at 2018 ESA Antenna Workshop in the Netherlands, the Best Paper Award in Electromagnetics and Antenna Theory at the 2018 European Conference on Antennas and Propagation (EuCAP), London, UK and the Best Antennas Paper Award at EuCAP 2021, Düsseldorf, Germany.